

Role of magnetic exchange energy on charge ordering in $R_{1/3}\text{Sr}_{2/3}\text{FeO}_3$ ($R = \text{La, Pr, and Nd}$)J. Ma,^{1,2,*} J.-Q. Yan,^{1,*} S. O. Diallo,^{1,*} R. Stevens,³ A. Llobet,³ F. Trouw,³ D. L. Abernathy,⁴
M. B. Stone,⁴ and R. J. McQueeney^{1,2}¹*Ames Laboratory, US-DOE, Ames, Iowa 50011, USA*²*Department of Physics and Astronomy, Iowa State University, Ames, Iowa 50011, USA*³*Los Alamos National Laboratory, Los Alamos, New Mexico 87545, USA*⁴*Oak Ridge National Laboratory, P.O. Box 2008, Oak Ridge, Tennessee 37831, USA*

(Received 25 July 2011; revised manuscript received 21 November 2011; published 22 December 2011)

Inelastic neutron scattering is applied to study the role of magnetism in stabilizing the charge-ordered state in $R_{1/3}\text{Sr}_{2/3}\text{FeO}_3$ (RSFO) ($R = \text{La, Pr, and Nd}$). The ratio of the ferromagnetic exchange energy J_F and antiferromagnetic exchange energy J_{AF} , $|J_F/J_{AF}|$, is a key indicator of the stability of the charge-ordered and antiferromagnetic ordered state. This ratio is obtained from the spin-wave spectrum by inelastic neutron scattering and is sufficiently large to suggest that the magnetic exchange energy alone can stabilize the charge-ordered state in $\text{La}_{1/3}\text{Sr}_{2/3}\text{FeO}_3$ and $\text{Pr}_{1/3}\text{Sr}_{2/3}\text{FeO}_3$. The exchange ratio decreases from $\text{La}_{1/3}\text{Sr}_{2/3}\text{FeO}_3$ to $\text{Nd}_{1/3}\text{Sr}_{2/3}\text{FeO}_3$, which indicates a gradual destabilization of the magnetic exchange mechanism for charge ordering in correspondence with the observed reduction in the ordering temperature.

DOI: [10.1103/PhysRevB.84.224115](https://doi.org/10.1103/PhysRevB.84.224115)

PACS number(s): 78.70.Nx, 75.25.Dk, 71.30.+h, 72.10.Di

I. INTRODUCTION

The charge-ordering (CO) transition is often encountered in complex transition-metal oxides (TMO) and has been the focus of intense inquiry and debate in condensed matter science in the past years. The metal-insulator transition that occurs as the temperature decreases across the CO transition temperature T_{CO} is associated with a change from an itinerant electronic state to a more localized state. The CO state plays an important role in various systems, including the superconducting cuprates and the proximity of the superconducting state to a spin/charge stripe ordered state,¹ colossal-magnetoresistive manganites, where the CO states compete with ferromagnetic metallic states² and layered nickelates, which form a small polaron lattice.³ Therefore, understanding the causes and implications of CO phenomena is significantly important. The CO state is also often closely associated with magnetic and orbital ordering, and it is widely recognized that CO can arise from a variety of competing interactions, most importantly the intersite Coulomb interaction, magnetic exchange energy, and electron-phonon interactions, all of which are strongly dependent on the valence states of neighboring metal ions.

The Sr-doped rare earth ferrite $R_{1/3}\text{Sr}_{2/3}\text{FeO}_3$ (RSFO) is an interesting example of a CO system where magnetic exchange energy is thought to play a crucial, if not dominant, role in the stability of the CO state. RSFO is a perovskite based crystal where the Fe ion adopts a formal fractional valence of 3.67+. Below T_{CO} , it has been proposed that charge disproportionation occurs according to $3\text{Fe}^{3.67+} \rightleftharpoons 2\text{Fe}^{3+} + \text{Fe}^{5+}$, with the different iron valences ordering in planes containing a repeating arrangement of 3+, 3+, 5+ ions perpendicular to the body diagonal $[111]_c$.^{4,5} The CO occurs simultaneously with an antiferromagnetic (AF) order. Recently, we used inelastic neutron scattering (INS) measurements of the spin-wave spectrum to demonstrate the plausibility that the magnetic exchange energy is the dominant interaction giving rise to CO in $\text{La}_{1/3}\text{Sr}_{2/3}\text{FeO}_3$ (LSFO).⁶ Our results show that the observed CO ground state can be stabilized by a large ferromagnetic (F) exchange energy

(J_F) occurring between the nearest-neighbor (NN) Fe^{3+} - Fe^{5+} pairs. However, this conclusion was made based on the assumption that the intersite Coulomb interaction (i.e., the Madelung energy) is suppressed by strong electronic screening enabled by the small charge-transfer (CT) gap (several to 10's of meV) observed in the system.⁶ Since we cannot directly determine the contribution of the Coulomb interaction, one possible way to verify the dominance of the magnetic exchange mechanism is to measure the magnetic exchange energies in other RSFO (for example, $R = \text{Pr}$ and Nd) compounds. For the smaller Pr^{3+} and Nd^{3+} ions, increased lattice distortions lead to a larger charge-transfer gap and a narrower electronic bandwidth. This should lead to reduced screening and increase the stability of the CO state due to a greater influence of the Coulomb interaction. However, T_N and T_{CO} are known to be suppressed by smaller R^{3+} .⁵ Mizokawa and Fujimori proposed that the $|J_F/J_{AF}|$ exchange ratio is a good indicator of the propagation direction of CO in the limit where magnetic energy is dominant. If the ratio is larger than 1, the charges will be ordered along $[111]$; if the ratio is less than 1, the charges will be ordered along $[100]$.⁷ Thus, if neutron scattering measurements can indicate a weakening of the magnetic exchange ratio, this would give additional support to the magnetic mechanism for CO.

To verify this hypothesis, we study the spin-wave spectrum in RSFO with different R^{3+} ions. Based on the INS measurement of the powder sample, the magnetic exchange energies, J_F and J_{AF} , can be obtained,⁸ and the related exchange ratio could be calculated. The corresponding contribution of the magnetic energy to the CO state could then be considered. However, the magnetic spectra of PSFO and NSFO are not as simple as that of the previously studied LSFO system,⁶ where only Fe moments contribute to the neutron magnetic cross section, as the Pr^{3+} and Nd^{3+} ions themselves possess magnetic moments. The neutron intensity from crystal electronic field (CEF) excitations of the magnetic Pr^{3+} and Nd^{3+} ions makes the extraction of the Fe spin-wave spectrum more complicated. To better account for the rare earth

CEF excitations, we also investigate the parent compounds, RFOs ($R = \text{Pr}$ and Nd). All of the RFO parent compounds are insulators with G -type antiferromagnetic ordering of Fe atoms occurring at high temperatures ($T_N \approx 700$ K). The rare earth ions in RFO are expected to have a similar CEF spectra to RSFO once the simple dilution of the rare earth site by Sr is taken into account. After accounting for the CEF intensities of the R^{3+} ions in the total magnetic cross section of an RSFO, the INS data may be compared to calculations of the spin-wave spectra and their corresponding cross sections using a Heisenberg model. We show that the ratio $|J_F/J_{AF}|$ is found to decrease with smaller R^{3+} which can account for the reduction in T_N by the magnetic mechanism.

II. EXPERIMENT

Polycrystalline RFeO_3 (RFO) and RSFO ($R = \text{La}$, Pr , and Nd) were prepared by a conventional solid-state reaction method. Stoichiometric amounts of La_2O_3 , or Nd_2O_3 , or Pr_6O_{11} , SrCO_3 , and Fe_2O_3 were mixed by grinding with mortar and pestle. The mixtures were transferred to an Al_2O_3 crucible and calcined several times in air at temperatures of 1100 and 1200 °C, respectively, for 24 h. Then, the press-formed pellets were sintered in air at 1250 and 1350 °C for 30 h, respectively. As the ionic size decreases from La to Nd, the RSFO compounds tend to be more oxygen deficient.⁹ PSFO and NSFO were annealed under oxygen pressure (10 bar) at 600 °C for 72 h. Room temperature powder x-ray diffraction (XRD) patterns were performed on a Rigaku Miniflex x-ray diffractometer with $\text{Cu } K_\alpha$ radiation to confirm phase purity. No impurities were observed. The oxidation state of iron was determined by iodometric titration and is listed in Table I.

The CO and AF transition temperatures for the Sr-doped samples were determined by neutron powder diffraction (NPD), using the High-Intensity Powder Diffractometer (HIPD) at the Lujan Center at Los Alamos National Laboratory, and zero field cooled (ZFC) magnetization measurements using a superconducting quantum interference device (SQUID) magnetometer. These characterization data are shown in Fig. 1. The RSFO systems were found to

have identical magnetic propagation vectors and charge-order propagation vectors (inferred via the development of structural superlattice peaks) below T_N . Figure 1(d) shows temperature dependent neutron diffraction data for PSFO and indicates the charge-order propagation vectors at $(n/6, n/6, n/6)$, where n is even, and magnetic propagation vectors at $(m/6, m/6, m/6)$, where m is odd.¹⁰ The lattice constants determined from refinement of the 300 K NPD and the magnetic transition temperatures are listed in Table I. The bond lengths and bond angles determined from NPD patterns at 300 K are listed in Table II. And the geometric tolerance factor t is expressed as

$$t = \frac{\langle R\text{-O} \rangle}{\sqrt{2}\langle \text{Fe-O} \rangle}, \quad (1)$$

where $\langle R\text{-O} \rangle$ and $\langle \text{Fe-O} \rangle$ are the average bond lengths of $R\text{-O}$ and Fe-O .

INS measurements were performed on Pharos spectrometer at the Lujan Center of Los Alamos National Laboratory and ARCS spectrometer at the Spallation Neutron Source (SNS) of Oak Ridge National Laboratory. Both instruments are direct geometry time-of-flight (TOF) spectrometers and measure the scattered intensity over a wide range of energy transfers $\hbar\omega$ and scattering angles between 1° and 140°, thereby allowing determination of a large swath of the scattering intensity $S(\mathbf{Q}, \omega)$ as a function of momentum transfer $\hbar\mathbf{Q}$ and energy transfer $\hbar\omega$, where \mathbf{Q} is the scattering vector.

On ARCS, powders (~ 14 g) of RFO and RSFO ($R = \text{La}$, Pr , and Nd) were packed in five aluminum foil sachets. The sachets were placed in an aluminum can filled with He exchange gas whose size was approximately $4.5 \times 6.5 \times 0.5$ cm. INS spectra were measured with an incident energy E_i of 180 meV. On Pharos, ~ 50 g of RFO and RSFO ($R = \text{La}$ and Nd) were packed in a flat aluminum can ($6 \times 6 \times 0.5$ cm), and the E_i 's were 120 and 160 meV. The face of the sample can was oriented at 135° to the incident neutron beam for both instruments in a transmission geometry. To achieve adequate statistics, the sample was measured for approximately ~ 24 h on Pharos, and ~ 5 h on ARCS. Empty sample can measurements were also performed and subtracted from the data presented.

TABLE I. Lattice and magnetic parameters of RFO and RSFO ($R = \text{La}$, Pr , and Nd) as determined by x-ray/neutron scattering measurements at 300 K, SQUID measurements T_N , and iodometric titration (oxygen deficiency).

	LaFeO_3	PrFeO_3	NdFeO_3
Space group	$Pnma$	$Pnma$	$Pnma$
Lattice constant (Å)			
a	5.56 ± 0.01	5.57 ± 0.01	5.59 ± 0.01
b	7.85 ± 0.02	7.79 ± 0.02	7.76 ± 0.02
c	5.56 ± 0.01	5.48 ± 0.01	5.45 ± 0.01
	$\text{La}_{1/3}\text{Sr}_{2/3}\text{FeO}_3$	$\text{Pr}_{1/3}\text{Sr}_{2/3}\text{FeO}_3$	$\text{Nd}_{1/3}\text{Sr}_{2/3}\text{FeO}_3$
Space group	$R\bar{3}c$	$R\bar{3}c$	$R\bar{3}c$
Lattice constant (Å)			
$a = b$	5.48 ± 0.01	5.48 ± 0.01	5.47 ± 0.01
c	13.41 ± 0.03	13.37 ± 0.03	13.34 ± 0.03
T_N (K)	210 ± 2.0	191 ± 2.0	189 ± 2.0
Oxygen stoichiometry	2.94 ± 0.03	2.97 ± 0.03	2.97 ± 0.03

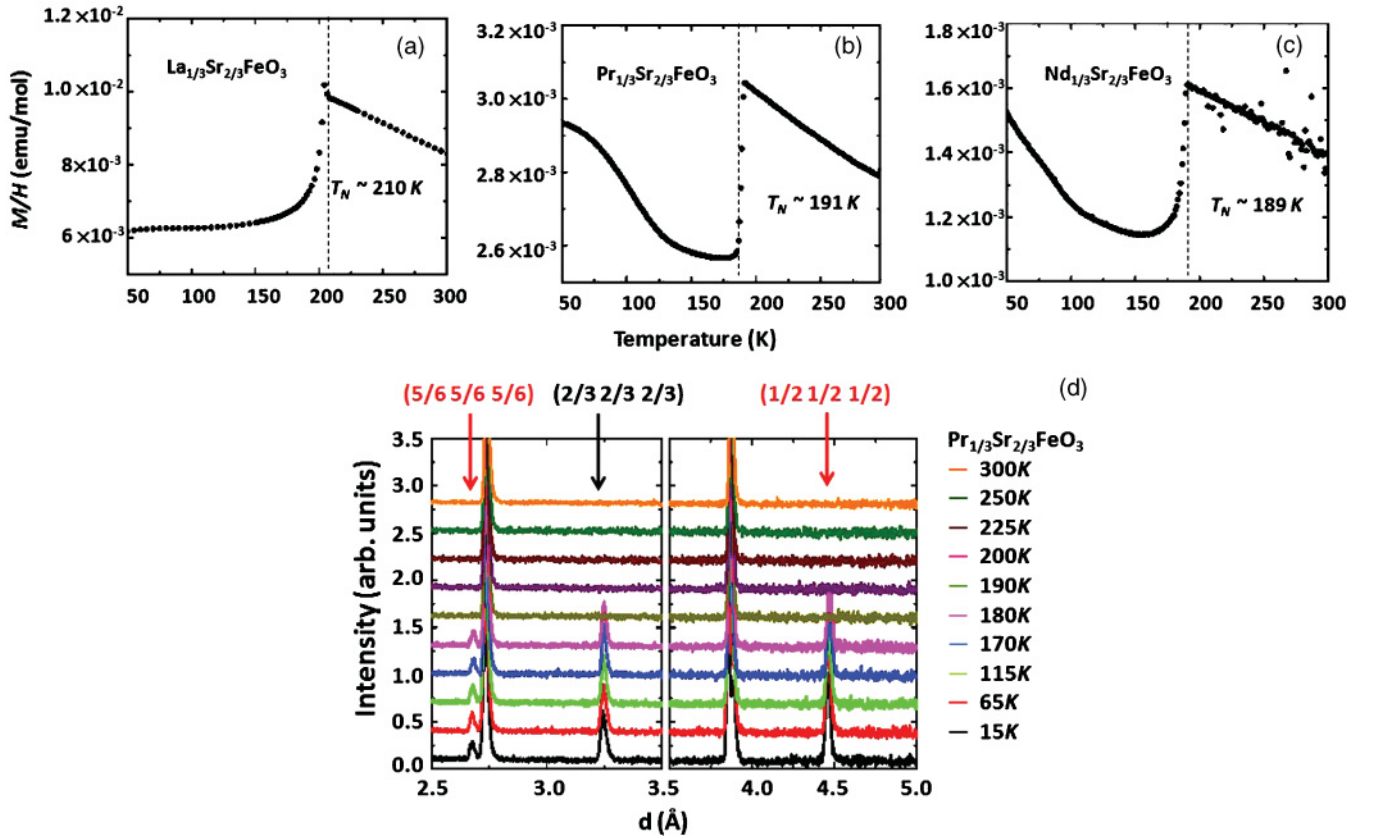


FIG. 1. (Color online) Magnetization of RSFO [R = (a) La, (b) Pr, and (c) Nd] as determined by ZFC SQUID measurements; (d) neutron powder diffraction of PSFO from 300 to 15 K as a function of d spacing. The arrows show the positions of the magnetic Bragg (red/light) and charged-ordered superlattice (black/dark) peaks.

III. RESULTS AND DISCUSSION

The unpolarized inelastic neutron scattering cross section contains contributions from both magnetic and phonon

scattering. In order to isolate the spin-wave spectrum, the magnetic scattering must first be separated from the phonon scattering. This is accomplished by using the fact that the magnetic scattering intensity decreases with Q (or 2θ) due to

TABLE II. The structural properties of RFO and RSFO as determined by NPD at 300 K.

	LaFeO ₃	PrFeO ₃	NdFeO ₃
Bond length (Å)			
$\langle R-O \rangle$	2.694 ± 0.008	2.627 ± 0.008	2.609 ± 0.008
Fe-O(1)	2.002 ± 0.004	2.004 ± 0.004	2.005 ± 0.004
Fe-O(2)	2.004 ± 0.004	2.006 ± 0.004	2.007 ± 0.004
Fe-O(2)	2.005 ± 0.004	2.015 ± 0.004	2.017 ± 0.004
Bond angle (°)			
\angle Fe-O(1)-Fe	157.6 ± 0.3	153.3 ± 0.3	151.2 ± 0.3
\angle Fe-O(2)-Fe	157.5 ± 0.3	152.4 ± 0.3	151.4 ± 0.3
Geometric tolerance factor			
t	0.951 ± 0.001	0.925 ± 0.001	0.918 ± 0.001
	La _{1/3} Sr _{2/3} FeO ₃	Pr _{1/3} Sr _{2/3} FeO ₃	Nd _{1/3} Sr _{2/3} FeO ₃
Bond length (Å)			
$R-O$	2.741 ± 0.006	2.738 ± 0.006	2.733 ± 0.006
Fe-O	1.940 ± 0.004	1.941 ± 0.004	1.939 ± 0.004
Bond angle (°)			
\angle Fe-O-Fe	173.2 ± 0.4	170.5 ± 0.3	169.3 ± 0.3
Geometric tolerance factor			
t	0.999 ± 0.002	0.997 ± 0.002	0.996 ± 0.002

the magnetic form factor, while the phonon scattering intensity increases proportionally to Q^2 .

The INS data of NdFeO₃ (NFO) taken on ARCS at $T = 10$ K with $E_i = 180$ meV are shown in Fig. 2(a) and used as an example of the data treatment. A similar analysis was performed for LaFeO₃ (LFO) on Pharos as outlined in Ref. 6. The data summed over the high angle range of $2\theta = 75^\circ\text{--}95^\circ$ contain primarily phonon scattering, Fig. 2(b), while the data within the low angle range $10^\circ\text{--}30^\circ$ contain scattering from both phonons and spin waves arising from the G -type AF order of Fe³⁺ and the CEF of Nd³⁺, Fig. 2(c). The magnetic scattering in NFO was isolated by subtracting the high angle phonon data from the low angle data after scaling the high angle data by a constant factor. A comparison of the scaled high angle data to the low angle data is shown in Fig. 2(c), and the phonon subtracted data is shown in Fig. 2(d). In order to compare the two instruments used for the INS measurements, the magnetic spectrum of NFO measured on Pharos is overplotted in Fig. 2(d). The spectra agree with each other very well.

A. Magnetic spectra of RFO

1. Fe spin waves

We now discuss the analysis of collective Fe spin waves below T_N in the parent RFO compounds. In RFO, NN Fe³⁺($3d^5$) spins are coupled by strong AF superexchange interactions ($J_{AF} < 0$). According to the single-crystal INS studies of TmFeO₃,¹² the spin waves can be approximated using a Heisenberg model Hamiltonian with only isotropic NN exchange interaction:

$$\mathbf{H} = -J_{AF} \sum_{\langle i,j \rangle} \mathbf{S}_i \cdot \mathbf{S}_j, \quad (2)$$

where \mathbf{S}_i and \mathbf{S}_j represent the spin vectors of the i th and j th iron atoms, respectively, that are NNs.

Therefore, the numerical calculations of the spin-waves cross section in the linear approximation to the Heisenberg model can be expressed as

$$\begin{aligned} \frac{d^2\sigma}{d\Omega d\omega} &= \frac{1}{2}(\gamma r_0)^2 \frac{k'}{k} \left(1 + \frac{(\hat{\mu} \cdot \mathbf{Q})^2}{Q^2} \right) \\ &\times \sum_n \left| \sum_i F_i(\mathbf{Q}) \sigma_i \sqrt{S_i} T_{ni}(\mathbf{q}) e^{-i\mathbf{Q} \cdot \mathbf{d}_i} \right|^2 \\ &\times [n(\omega) + 1] \delta(\omega - \omega_n(\mathbf{q})), \end{aligned} \quad (3)$$

where $\mathbf{Q} = \vec{k}' - \vec{k}$ is the scattering vector, and $\hbar\omega$ is the energy transfer. \vec{k} and \vec{k}' are the initial and final neutron wave vectors, respectively. The i th spin \mathbf{S}_i pointed in direction $\hat{\mu}$ is located at position \mathbf{d}_i . The symbol $\sigma = \pm 1$ is the direction of the spin relative to the quantization axis $\hat{\mu}$ for a collinear spin structure. The symbol $\mathbf{q} = \mathbf{Q} - \tau$ is the spin-wave wave vector in the 1st Brillouin zone. $T_{ni}(\mathbf{q})$ is the spin-wave eigenvector, and $F_i(\mathbf{Q})$ is a product of the Lande g -factor, magnetic form factor, and Debye-Waller factor for the i th spin. Finally, $n(\omega)$ is the temperature dependent Bose factor.

The INS information obtained from the polycrystalline samples is related to the spin-wave density-of-states (SWDOS) via a powder averaging over all crystallographic directions.⁸ For the G -type LFO spin waves, the SWDOS consists of a

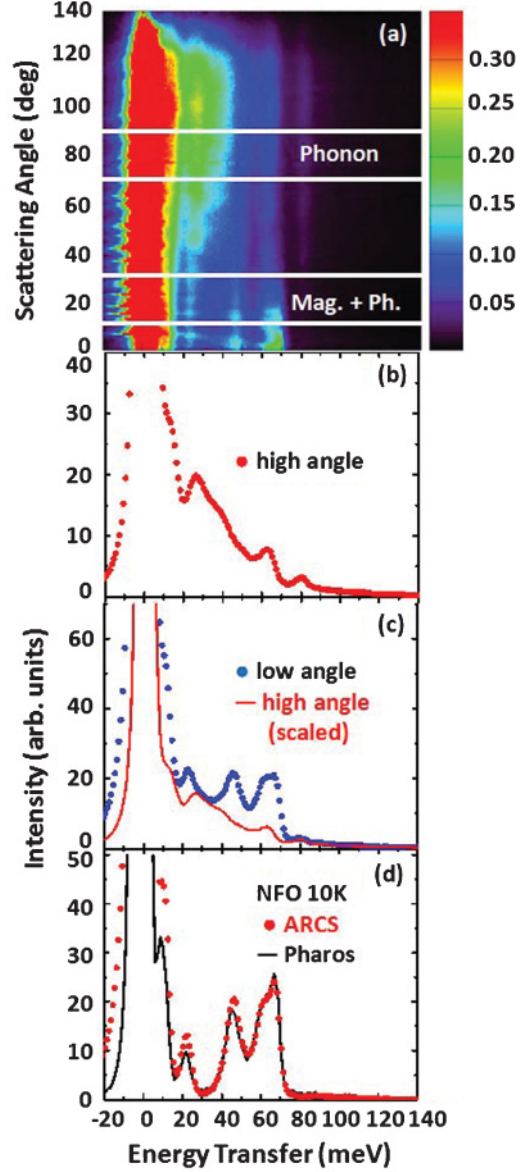


FIG. 2. (Color online) (a) Inelastic neutron scattering intensity ($E_i = 180$ meV) of NFO (color scale) vs scattering angle and energy transfer at $T = 10$ K as measured at ARCS. Horizontal white lines delineate regions where phonon and magnetic scattering are isolated; (b) neutron intensity summed over the angular range $75^\circ\text{--}95^\circ$ originating from phonons (red dots); (c) neutron intensity summed over the low angular range $10^\circ\text{--}30^\circ$ (blue dots), and phonon background scaled from the high angle sum; (d) the isolated magnetic scattering of ARCS data (red dots) and Pharos data (black line).

single sharp peak at an energy of $6|J_{AF}|S^{3+}$, and S^{3+} is the spin magnitude of Fe³⁺ ion. Assuming $S^{3+} = 5/2$, a value of $J_{AF} = -4.9$ meV can be determined from the position of this single peak at 73 meV, shown in Fig. 3. The value of J_{AF} is also listed in Table III.

Figure 3 shows the phonon subtracted magnetic data for LFO, PrFeO₃ (PFO), and NFO found via the procedure described in Fig. 2. As La³⁺ has no f electrons, there are no CEF excitations existing in LFO. While PFO and NFO have similar G -type magnetic structures as LFO, it is clear

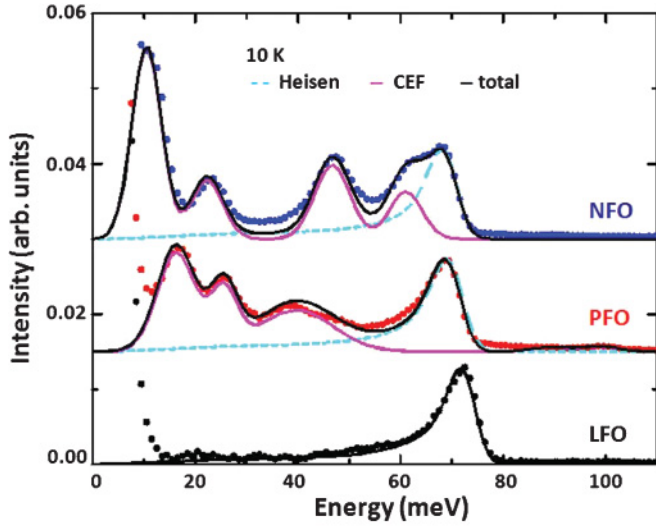


FIG. 3. (Color online) The experimental angle-averaged magnetic INS data for RFO ($R = \text{La, Pr, and Nd}$) on ARCS at 10 K and $E_i = 180$ meV (dots). Heisenberg model calculation of the powder-averaged Heisenberg spin-waves cross-section (Heisen) for G -type magnetic order are shown as dash cyan lines, and black/dark line for LFO. Additional peaks in the spectra for $R = \text{Pr and Nd}$ and associated solid pink/light lines are the fits of CEF excitations.

that the neutron spectra of PFO and NFO contain additional magnetic excitations due to R^{3+} CEF excitations which will be discussed later. In order to determine which of the observed peaks are due to Fe spin waves and which are CEFs, we can use mean-field theory and knowledge of T_N to estimate the J_{AF} exchange coupling between Fe ions for $R = \text{Nd and Pr}$. In mean-field theory,¹³

$$3k_B T_N = N |J_{AF}| \sqrt{S(S+1)}, \quad (4)$$

where $N = 6$ and S is the spin angular momentum, $5/2$.⁸ With this assumption, the magnetic exchange energies are expected to weaken slightly upon going from LFO to NFO due to the decrease of T_N . However, it is well known that T_N is overestimated in mean-field theory, and therefore the mean-field estimate of the exchange is smaller than that observed by neutron scattering. Table III lists the AF exchange energy based on Eq. (4). A more accurate value of the exchange can then be obtained by fitting the SWDOS peak in the INS data by the Heisenberg model, Eq. (3). Since the magnetic inelastic spectrum of LFO only includes the contribution of Fe^{3+} , it is easy to calculate the J_{AF} , which is -4.9 meV. Furthermore, Eq. (4) also establishes a proportionality between T_N and J_{AF} . Hence, we could estimate the J_{AF} of PFO and

NFO based on our knowledge of the J_{AF} of LFO and the Neel transition temperatures of all three compounds. The results are listed Table III. Then, the LFO related J_{AF} 's of PFO and NFO are good references for the Fe^{3+} SWDOS simulation by Eq. (3), and the final fittings are shown in Fig. 3. According to superexchange theory, crystalline distortions caused by the smaller rare earth ions result in a bending of the Fe-O-Fe bond angle that weakens J_{AF} , Table II.¹⁴

2. Crystal electric fields of Pr^{3+} and Nd^{3+}

Mean-field theory helps us locate the characteristic energy of spin-wave excitations from the Fe^{3+} ions. The remaining excitations in the phonon subtracted data should be from the CEF of R^{3+} ions. The cross section for CEF excitations can be written as¹⁵

$$\frac{d^2\sigma}{d\Omega d\omega} \propto [g_J F(\mathbf{Q})]^2 e^{-2W} \frac{k'}{k} S_{\text{CEF}}(\mathbf{Q}, \omega), \quad (5)$$

where g_J is Lande factor of the R^{3+} ion, $F(\mathbf{Q})$ is the R^{3+} magnetic form factor, and e^{-2W} is the R^{3+} Debye-Waller factor. $S_{\text{CEF}}(\mathbf{Q}, \omega)$ is the response function of the system which is determined by the temperature, CEF level splitting, CEF eigenstates, and corresponding CEF matrix elements:

$$S_{\text{CEF}}(\mathbf{Q}, \omega) = \sum_{i,j} \rho_i |\langle i | \mathbf{J}_\perp | j \rangle|^2 \delta(E_i - E_j - \hbar\omega), \quad (6)$$

where $|i\rangle$ and $|j\rangle$ are the initial and final CEF eigenstates of the system with level energies E_i and E_j . The operator \mathbf{J}_\perp is the component of the total angular momentum perpendicular to the scattering vector; ρ_i is the thermal population factor of the initial state. Observable excitations occur between levels which have nonzero matrix elements.

For rare earth ions, the spin-orbit coupling is usually stronger than the CEF potential, and the total angular momentum $\mathbf{J} = \mathbf{L} + \mathbf{S}$ remains a good quantum number. Therefore, the magnetic form factor in Eq. (5) is given by^{15,16}

$$F(\mathbf{Q}) = \langle j_0(Q) \rangle + \langle j_2(Q) \rangle \times \frac{J(J+1) + L(L+1) - S(S-1)}{3J(J+1) + S(S-1) - L(L+1)}, \quad (7)$$

where $\langle j_0 \rangle$ and $\langle j_2 \rangle$ are Q -dependent functions whose values are tabulated.¹⁷

a. NdFeO₃. The ground state of the free Nd^{3+} ion has 3 unpaired f electrons, and the Russell-Saunders term symbol is $^4I_{9/2}$ with a degeneracy of $2J+1 = 10$. At a point of orthorhombic symmetry in the distorted perovskite cell, the ground state multiplet splits into $(2J+1)/2 = 5$ CEF

TABLE III. Magnetic exchange energy and T_N of RFO ($R = \text{La, Pr and Nd}$).

	LaFeO ₃	PrFeO ₃	NdFeO ₃
T_N (K) ¹¹	738	707	693
Mean field [J_{AF} (meV)]	-3.74	-3.58	-3.51
Heisenberg model	-4.9	-4.69	-4.60
(J_{AF} (meV) based on LFO)			
Heisenberg model [J_{AF} (meV), fitted]	-4.9	-4.55	-4.45

doublets.¹⁶ At 10 K, we observe four CEF transitions at ~ 9 , 21, 46, and 60 meV as shown in Fig. 3. These are consistent with previous work,^{18,19} and are associated with excitations from the CEF ground state to each of the four excited states. Due to the possible overlap of CEF excitations with spin waves, the phonon scattering contribution, and multiple scattering, the separation of the CEF contribution was done by examining both the ω - and Q -dependence of the total cross section. The positions and integrated intensities of the Nd^{3+} CEFs in NFO at 10 K were determined by

$$S(Q, \omega) = S_{\text{mag}}(Q, \omega) + S_{\text{phonon}}(Q, \omega) + S_{\text{CEF}}(Q, \omega) + S_{\text{bkg}}(Q, \omega), \quad (8)$$

where $S_{\text{mag}}(Q, \omega)$ is the polycrystalline averaged spin-wave scattering of Fe^{3+} ions, $S_{\text{phonon}}(Q, \omega)$ is the polycrystalline-averaged phonon background, $S_{\text{CEF}}(Q, \omega)$ is the CEF scattering from Nd^{3+} ions, and $S_{\text{bkg}}(Q, \omega)$ is the background scattering which is assumed to be a constant as a function of Q and some energy dependence.

For simplicity, we treat the phonon scattering from a powder sample in the incoherent approximation. In this approximation, the one-phonon scattering is proportional to the phonon density-of-states (DOS) and can be expressed as

$$S_{\text{inc}, \pm 1 \text{phonon}}(\mathbf{Q}, \omega) = \frac{Q^2}{\hbar \omega} Z(\hbar \omega) \langle n + 1 \rangle, \quad (9)$$

where $Z(\hbar \omega)$ is the sum of the weighted partial phonon DOS, $Z_i(\hbar \omega)$:

$$Z(\hbar \omega) = \sum_i \frac{b_i^2}{2M_i} e^{-2W_i} Z_i(\hbar \omega), \quad (10)$$

and $\langle n + 1 \rangle$ is the Bose population factor:

$$\langle n + 1 \rangle = \frac{1}{2} \left[\coth \left(\frac{1}{2} \hbar \omega \beta \right) + 1 \right], \quad (11)$$

The constant energy scans obtained from averaging over different energy transfer ranges are shown in Fig. 4. Figure 4(a) is averaged over an energy range 10.5–20.5 meV and is described here as an example. The background contributions (bkg) are treated as a constant background (horizontal line). The single phonon (ph.) cross section is determined by assuming an incoherent quadratic Q dependence (parabolic curve) given by Eq. (9). In order to compare with the reported data in Refs. 18 and 19, the CEF excitation data were integrated from 1.6 to 4.8 \AA^{-1} , which corresponds approximately to the scattering angle range from 10° to 30° . Furthermore, we note that the peaks seen at high Q (above 5 \AA^{-1}) arise from coherent phonon scattering that is not included in the analysis. The spin-wave scattering intensities (Heisen) of Fe^{3+} are calculated from a Heisenberg model (zigzag line). Note that the sharp peaks in the spin-wave contribution arise from the coherent scattering, which is included in the Heisenberg model

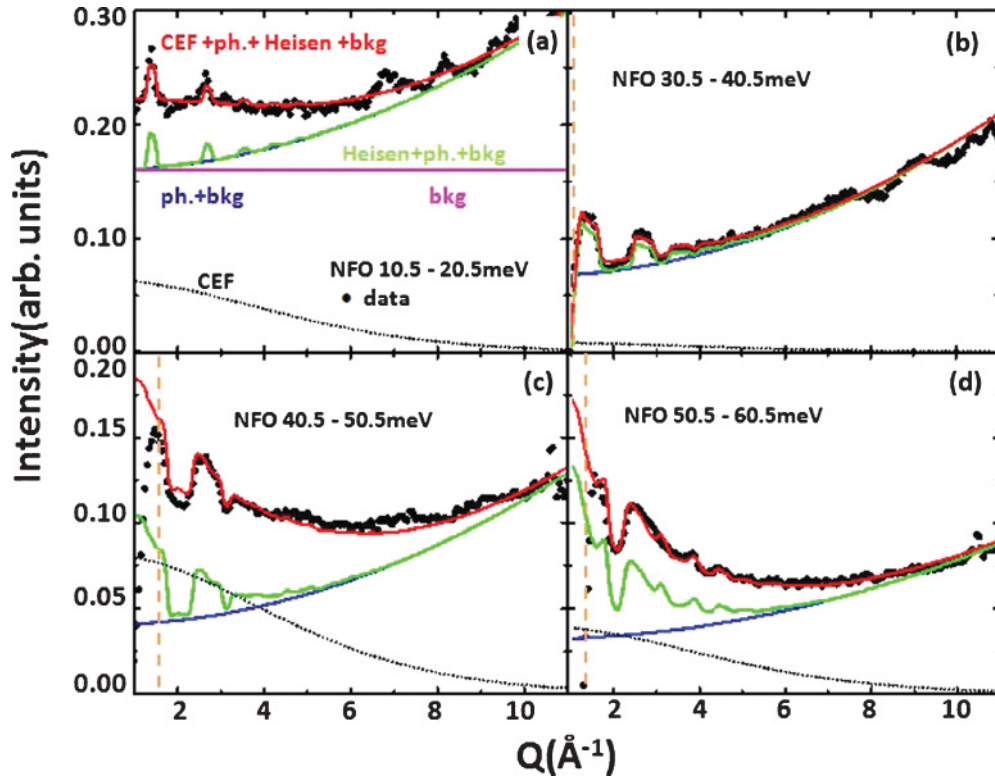


FIG. 4. (Color online) The Q dependence of the neutron scattering data averaged over different energy transfer ranges in NFO on ARCS at 10 K and $E_i = 180$ meV. (a) 10.5–20.5, (b) 30.5–40.5, (c) 40.5–50.5, and (d) 50.5–60.5 meV. The black dots are the experimental data. The blue lines are estimates of the incoherent phonon background (ph.) plus the background scattering (bkg). The green lines are the calculations of the polycrystalline averaged spin-wave scattering (Heisen) plus the background using the parameters in the text. The red lines are sums of the calculations of the CEF, the polycrystalline averaged spin-wave scattering, the background, and multiple scattering. The vertical brown dashed lines in (b) to (d) are the usable low-angle data limits of the experiment. The dotted lines are the fitted CEF excitations.

TABLE IV. The measured and calculated CEF transition energies and integrated intensities of Nd³⁺ in NFO at 10 K.^{18,19}

E_{j0}	$\hbar\omega$ (meV)		Integrated intensities	
	Calculated	Measured	Calculated	Measured
E_{10}	10.1	9.4 ± 0.1	100.0	100.0 ± 3.1
E_{20}	22.4	21.2 ± 0.1	29.3	30.9 ± 1.1
E_{30}	44.7	45.7 ± 0.1	46.1	41.8 ± 1.6
E_{40}	60.8	59.9 ± 0.1	7.0	17.8 ± 1.3

calculations of the powder-averaged cross section. Especially at low energies, the sharp inelastic peaks are coincident with the position of magnetic Bragg peaks. The remaining signal is associated with CEF scattering, which follows the magnetic form factor. The energy ranges where there is a large difference between total fitting line (background + phonon + spin wave) and the data signals the presence of a CEF excitation. The dotted line in Fig. 4 is the fitted CEF intensities.

The measured and calculated transition energies and integrated intensities of the CEF levels are listed in Table IV and plotted in Figs. 3 and 4. The transition energy between different energy levels is defined as E_{ji} , which j th and i th label the energy levels. The CEF excitations of NFO can be found in Refs. 18 and 19. The calculation and measurement of the CEF transitions agree with each other very well. If we normalize the intensities of the CEF transitions to the intensity of the excitation from the ground state to the first excited state, which are 9.4 and 10.1 meV for the measurement and calculation, respectively, the measured intensities of the second (~ 21.2 meV) and third excited states (~ 45.7 meV) agree with the calculations based on estimates of the corresponding matrix elements. A comparison of the intensity of the 59.9 meV state is more difficult due to the proximity to the magnetic signal from Fe³⁺ spin waves.

b. PrFeO₃. We next examine the CEF transitions in PFO. Although many experimental and theoretical studies on Pr³⁺ in perovskite oxides have been performed,^{20,21} we know of no complete set of experimental data for CEF levels of Pr³⁺ ions in the perovskite structure. There are 2 unpaired f electrons for Pr³⁺, and the electronic term is 3H_4 . Since the structure of

PFO is orthorhombically distorted and $J = 4$, the ground state multiplet splits into $2J + 1 = 9$ singlets. The dipole allowed transitions from the ground state are listed in Table V. Similar to the analysis of NFO, the magnetic form factor of Pr³⁺ in PFO is taken from the literature¹⁷ and used with the previously observed transitions from Ref. 20 in Table V to establish the fraction of different contributions to the total cross section. Figure 5 shows the result of the process. The data agree well with the model calculation over a range of wave vector and energy transfers.

The CEF levels in PFO were compared to those of Pr³⁺ in PrGaO₃ (PGO) because it had a Pr³⁺ CEF scattering similar to PFO and was the only theoretical calculation on the CEF of Pr³⁺ in perovskite oxides with the space group *Pnma*.^{20,21} There are discrepancies between our measurements of CEF excitations in PFO and the calculations for PGO. First, the CEF transition predicted to appear around ~ 67 meV was not observed in our measurement. This is likely due to the proximity of this transition to the Fe³⁺ spin-wave band. The proposed observation of this CEF transition was mentioned in regards to INS measurements of PFO and PGO.^{20,21} However, this analysis did not report the spin-wave excitation of Fe³⁺ ions,²¹ and the magnetic peak claimed to be a CEF around ~ 60 meV is much more likely to be Fe³⁺ spin-waves scattering. An examination of Fig. 5(e) shows that the 67 meV CEF transition may be either too weak to observe (as compared to the Fe³⁺ spin waves) or shifted in energy as compared to PGO. We also observe a weak excitation peak around ~ 100 meV, Fig. 3. This is presumably a CEF excitation; however the matrix element is predicted to be zero.²⁰

TABLE V. The measured and calculated CEF transition energies and integrated intensities of Pr³⁺ in PFO at 10 K.

E_{j0}	PrFeO ₃ (measured)		PrGaO ₃ (calculated)	Integrated intensities (present work)
	Ref. 20	present work	Ref. 21	
E_{10}	2.0 ± 0.1		5.6	
E_{20}	14.7 ± 0.4	15.2 ± 0.1	16.0	100.0 ± 3.1
E_{30}	23.2 ± 0.5	24.7 ± 0.1	23.4	41.1 ± 1.6
E_{40}	36.0 ± 1.0	36.6 ± 0.5	32.9	82.2 ± 2.3
E_{50}	58.0 ± 2.0		67.4	
E_{60}			69.3	
E_{70}		80.1 ± 0.5	89.5	4.2 ± 0.8
E_{80}		97.9 ± 0.3	113.1	4.9 ± 0.5

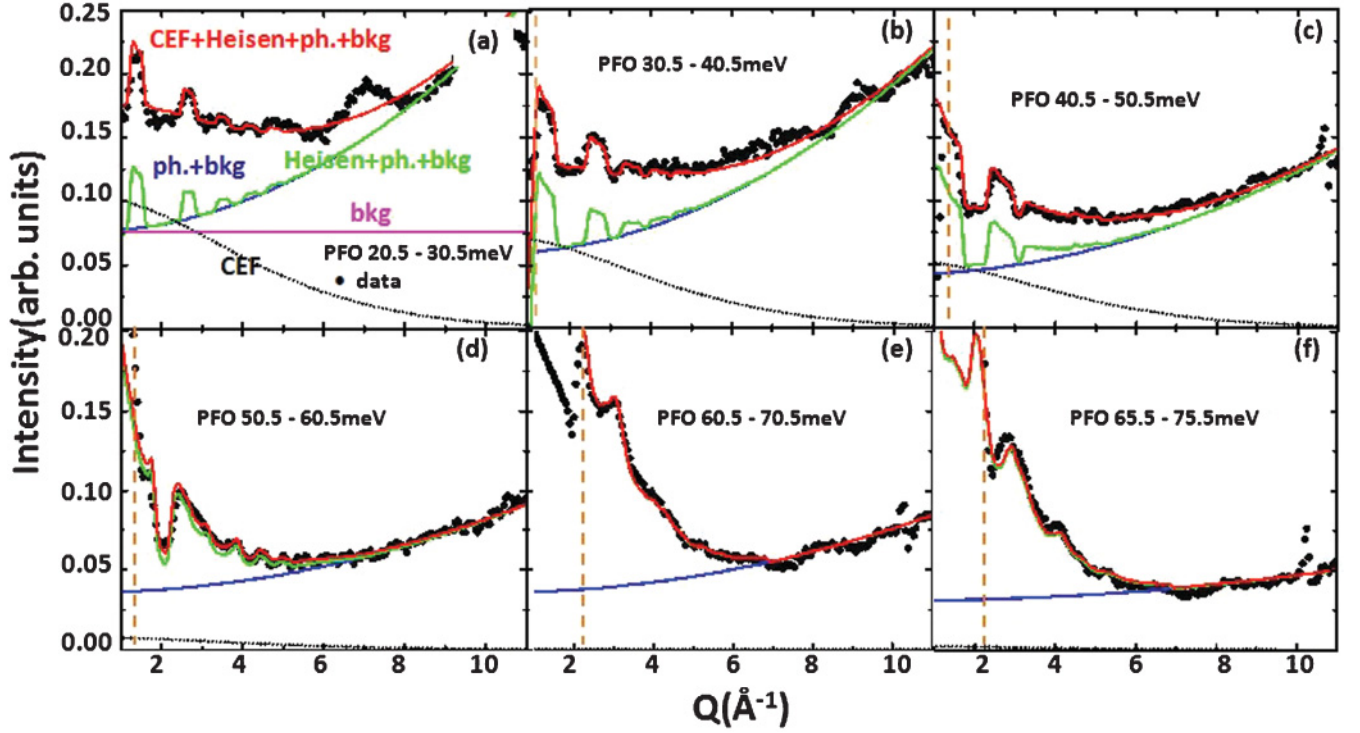


FIG. 5. (Color online) The Q dependence of the neutron scattering data for different energy transfer ranges (Q cuts) in PFO on ARCS at 10 K and $E_i = 180$ meV. The brown dashed lines in panels (b), (c), (d), (e), and (f) indicate the usable low-angle data limits of the experiment. The dotted lines are the fitted CEF excitations.

B. Magnetic excitations in RSFO

We now take our knowledge of the differential scattering cross sections in the parent RFO compounds and use it in an attempt to isolate the scattering arising from the Fe spin waves in the doped RSFO compounds, Fig. 6(a). As Sr ions are introduced into LFO, the magnetic intensity of LSFO in the CO phase at $T = 10$ K is split into two bands, Fig. 6(b).

Figure 7(a) shows the extracted low-angle magnetic intensity of RSFO ($R = \text{La, Nd, and Pr}$). In general, we find magnetic signals up to a maximum energy of 120 meV. The high energy portion of the magnetic excitation spectrum

between 90 and 120 meV is very similar for each compound. In LSFO, this high energy band is associated with spin waves propagating in ferromagnetic channels in the magnetic lattice. The low energy features are more difficult to compare due to the presence of R^{3+} CEF excitations.

1. Crystal electric fields of Pr^{3+} and Nd^{3+}

The CEF information obtained from the parent RFO compounds ($R = \text{Pr and Nd}$) can be used as a guide to estimate the CEF contribution in Sr-doped RSFO. Because the ionic radius of Sr^{2+} is close to the radii of the R^{3+} ion, we assume

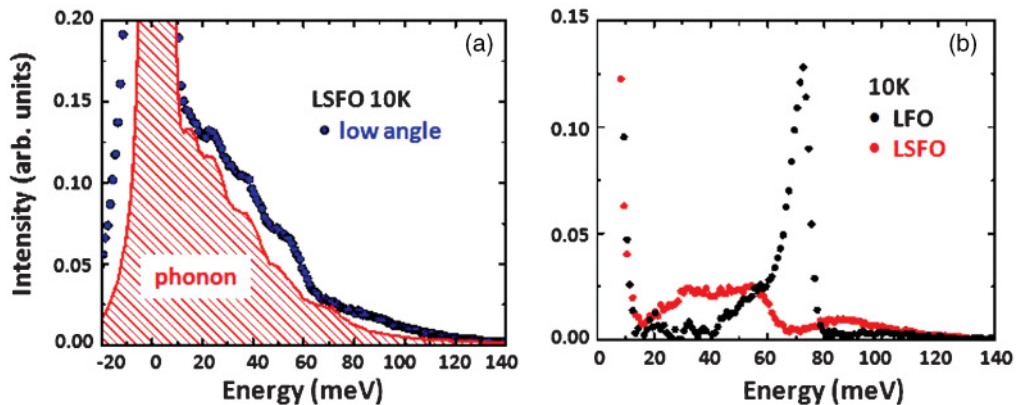


FIG. 6. (Color online) (a) Neutron intensity summed over the low angular range 10° – 30° (blue dots) and phonon background scaled from the high angle sum of LSFO (color scale) vs energy transfer at $T = 10$ K at ARCS with $E_i = 180$ meV; (b) the isolated magnetic scattering of LFO (black/dark dots) and LSFO (red/light dots).

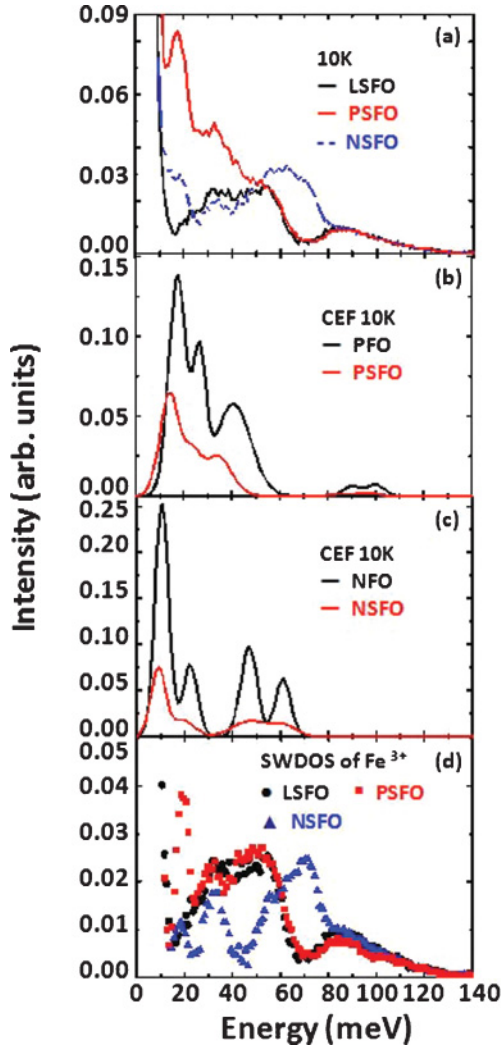


FIG. 7. (Color online) (a) Magnetic inelastic neutron scattering intensity of *RSFO* ($R = \text{La}$ (black/dark solid line), Pr (red/light solid line), and Nd (blue/light dash line)) vs energy transfer on ARCS at $T = 10 \text{ K}$ and $E_i = 180 \text{ meV}$. The calculated CEF intensities of (b) PFO (black/dark line) and PSFO (red/light line), and (c) NFO (black/dark line) and NSFO (red/light line). (d) The spin-wave scattering from Fe ions in *RSFO* [$R = \text{La}$ (black dark circles), Pr (red/light squares), and Nd (blue/light triangles)] found via a difference of the total magnetic signal (a) minus the fitted CEF contributions of (b) and (c), respectively.

that the average structural environment of the R^{3+} site does not change significantly in *RSFO* with Sr^{2+} doping. Thus, the CEF of R^{3+} in *RSFO* would be similar to that of *RFO*. Since $2/3$ of R^{3+} has been substituted by nonmagnetic Sr^{2+} ions, the integrated intensity of the CEF excitations in *RSFO* should be one-third of that found for *RFO*. However, the effect of disorder and other lattice distortions arising from the Sr^{2+} substitution may shift the position and broaden the width of CEF excitations.

The CEF scattering intensities of *RSFO* were fitted with the same method as used for the *RFO* samples. The intensities were initially constrained to be one-third of the corresponding transition in *RFO* and then allowed to vary in the final fits.

The fitted results of R^{3+} CEFs in the *RSFO* compounds are compared with the data of *RFO* in Figs. 7(b) and 7(c). The integrated intensities of the R^{3+} CEF states in these compounds are listed in Tables VI (Pr^{3+}) and VII (Nd^{3+}), respectively.

The integrated intensity ratio of the CEF excitations of Nd^{3+} in NFO is consistently three times that of the CEFs measured in NSFO as shown in Table VII. For PSFO, the ratio of Pr^{3+} CEF intensities deviates from 3 for the E_{20} transition, which overlaps the strong elastic peak.

2. Fe spin-wave excitations

After subtracting the CEF intensities for the *RSFO* compounds, the spin-wave excitations of Fe ions in all three *RSFO* compounds were isolated and are compared in Fig. 7(d). The spin-wave spectra in all three compounds agree with each other for energies greater than 85 meV. At all other energies, the spin-wave spectra of LSFO and PSFO remain similar: there are two energy bands with a gap between 60 and 80 meV. In NSFO, the low energy spectral weight appears to move to higher energies and fills this portion of the spectrum. The intense peaks around 20 and 30 meV in NSFO are signals which also exist in both LSFO and PSFO and are likely artifacts due to inaccuracies in subtracting the phonon spectra based upon high angle measurements.

Previous analysis of spin waves in LSFO⁶ showed that the spectrum can be modeled adequately for energy transfers above 40 meV where phonon corrections are modest. We base our model on the facts that there are two different kinds of Fe ions, Fe^{3+} and Fe^{5+} , and two nearest-neighbor exchange interactions which obey the Goodenough-Kanamori rules for the sign of the exchange; antiferromagnetism between half-filled Fe^{3+} - Fe^{3+} pairs and ferromagnetism between half-filled and empty e_g orbitals in Fe^{3+} - Fe^{5+} pairs, Figs. 8(a) and 8(b). Hence, the spin waves from the *RSFO* magnetic structure must be calculated numerically by the NN Heisenberg model, and the Hamiltonian is

$$\mathbf{H} = -J_{AF} \sum_{\langle i,j \rangle} \mathbf{S}_i^{3+} \cdot \mathbf{S}_j^{3+} - J_F \sum_{\langle i,j \rangle} \mathbf{S}_i^{3+} \cdot \mathbf{S}_j^{5+}, \quad (12)$$

where the sums are over each pair type, \mathbf{S}_i and \mathbf{S}_j represent the spin vectors of the i th and j th iron atoms of the type indicated, and the sums are over nearest-neighbor pairs with pairwise exchange values (J_F or J_{AF}) determined by the charge-ordered structure.

Hence, the spin-wave dispersions will be

$$\omega(\mathbf{q}) = 2S\{(2 | J_{AF} | + J_F)^2 - [2 | J_{AF} | \gamma_+(\mathbf{q}) + J_F \gamma_z(\mathbf{q})]^2\}^{1/2}, \quad (13)$$

where $\gamma_+(\mathbf{q}) = \frac{1}{2} (\cos q_x a + \cos q_y a)$, $\gamma_z(\mathbf{q}) = \cos q_z a$, \mathbf{q} is the spin-wave momentum, and a is the cubic perovskite lattice constant.

Because of the small charge-transfer gap in *RSFO*, significant hybridization exists between Fe and O resulting in some fractions of doped holes residing on the oxygen site. Even considering the presence of doped holes, the exchange between Fe^{3+} and nominal Fe^{5+} ions remains ferromagnetic. In the limit where the holes are on the iron site (corresponding

TABLE VI. The transition energies and integrated intensities (area) of Pr^{3+} CEF transitions in PFO and PSFO at 10 K. The last column shows ratios of the integrated intensities of the related excitations.

E_{j0}	PFO		PSFO		PFO/PSFO
	$\hbar\omega$ (meV)	area	$\hbar\omega$ (meV)	area	
E_{10}					
E_{20}	15.2 ± 0.1	1.29 ± 0.04	13.9 ± 0.3	0.68 ± 0.01	1.9 ± 0.1
E_{30}	24.6 ± 0.1	0.53 ± 0.02	23.3 ± 0.2	0.19 ± 0.01	2.9 ± 0.2
E_{40}	38.6 ± 0.5	1.06 ± 0.03	34.1 ± 0.1	0.36 ± 0.01	2.9 ± 0.1
E_{50}					
E_{60}					—
E_{70}	88.1 ± 0.5	0.054 ± 0.01	85.9 ± 0.4	0.018 ± 0.003	3.0 ± 0.4
E_{80}	97.9 ± 0.3	0.063 ± 0.07	96.9 ± 0.4	0.021 ± 0.002	3.0 ± 0.4

to full Fe^{5+} valence), F exchange occurs between half-filled and empty e_g orbitals according to the Goodenough-Kanamori rules. In the limit where a single hole is on the oxygen site, sharing of the spin-polarized oxygen electron also leads to a F exchange. For the same reason, if there is no distortion existing in the lattice, the presence of oxygen holes between Fe^{3+} - Fe^{3+} pairs will reduce J_{AF} as compared to the parent insulator RFO. NSFO is an exception and will be discussed later. Furthermore, the spin values of Fe ions are affected by hybridization: if the hole is on the oxygen ion, the Fe oxidation state is lower, and the effective spin of the Fe ions would be larger.

Figures 8(c) and 8(d) show the fitting results of PSFO and NSFO to the Heisenberg model of Eq. (12). Unlike the simple case of RFO, the fitting of NN Heisenberg model calculations and CEF excitations in RSFO does not show quantitative agreement with the data especially at low energies where phonon corrections are more important. However, as explained in Ref. 6 the critical ratio $|J_F/J_{AF}|$ can be estimated by the splitting between the upper (>70 meV) and lower energy (<60 meV) bands. For LSFO and PSFO, the NN Heisenberg model calculations show that these two main spin-wave bands originate from F-like/AF-like spin waves that propagate along/between the metal centered domain wall, respectively. Rough estimates of the energy scale for these excitations are

$$E_F \sim 3J_F(2S^{3+} + S^{5+}), \quad (14a)$$

$$E_{AF} \sim 3|J_{AF}|S^{3+} + 3J_FS^{5+}, \quad (14b)$$

Based on the previous reports on spin magnetic moments for different Fe ions, S^{3+} is very stable and keeps as its value

$5/2$, while S^{5+} is likely to be larger than the atomic limit of $3/2$ due to hybridization and can be adjusted.^{22,23} The final fitting of the magnetic exchange energies are shown in Table VIII.

The measured magnetic exchange ratio of J_F and $|J_{AF}|$ can be compared to the theoretical predictions of the magnetic exchange mechanism for the CO in RSFO ($R = \text{La, Pr, and Nd}$) as shown in Fig. 9. In the magnetic exchange only model proposed by Mizokawa *et al.*,⁷ two charge-ordered patterns are considered with alternating charge and spin ordering along either the (111) or (100) directions. Those with the observed pattern of charge ordering along the cubic (111) direction are stable for large values of the exchange ratio, $|J_F/J_{AF}| > 1$, although the boundary between the two phases at $T = 10$ K depends on the value of the NN exchange between Fe^{5+} - Fe^{5+} ions (J_{55}) that is present only in the (hypothetical) (100) charge-ordered structure. According to the Goodenough-Kanamori rules, it is expected that this exchange is weakly AF due to the π bonding of half-filled t_{2g} orbitals. In the limit where $J_{55} \approx 0$, the (111) order is stable when $|J_F/J_{AF}| > 1/2$. A much more conservative estimate of $J_{55} \approx |J_{AF}|$ results in the condition $|J_F/J_{AF}| > 1$ for the stability of (111) charge order. LSFO and PSFO have exchange ratios that clearly favor the (111) ordering, even in the most conservative estimate for the value of J_{55} . On the other hand, the exchange ratio for NSFO is slightly less than 1. This suggests that the (111)-type charge ordering is less stable in NSFO as compared to LSFO or PSFO. This is consistent with the suppression of T_N in the RSFO compounds.

The reduction of the exchange ratio in NSFO largely arises from a $\sim 20\%$ increase of $|J_{AF}|$ as compared to LSFO and

TABLE VII. The transition energies and integrated intensities (area) of Nd^{3+} CEF transitions in NFO and NSFO at 10 K. The last column shows ratios of the integrated intensities of these excitations.

E_{j0}	NFO		NSFO		NFO/NSFO
	E (meV)	area	E (meV)	area	
E_{10}	9.1 ± 0.1	1.8 ± 0.1	9.1 ± 0.4	0.6 ± 0.1	3.0 ± 0.3
E_{20}	20.8 ± 0.1	0.6 ± 0.1	19.2 ± 0.2	0.2 ± 0.1	3.0 ± 0.4
E_{30}	45.2 ± 0.1	0.9 ± 0.1	46.9 ± 0.4	0.3 ± 0.1	3.0 ± 0.5
E_{40}	59.5 ± 0.2	0.5 ± 0.1	60.9 ± 0.4	0.2 ± 0.1	3.1 ± 0.8

TABLE VIII. Parameters of the NN Heisenberg model for *RSFO* ($R = \text{La, Pr, and Nd}$) and the size of the charge-transfer gap.^{5,24} Parameters of LSFO are from Ref. 6.

	$\text{La}_{1/3}\text{Sr}_{2/3}\text{FeO}_3$	$\text{Pr}_{1/3}\text{Sr}_{2/3}\text{FeO}_3$	$\text{Nd}_{1/3}\text{Sr}_{2/3}\text{FeO}_3$
Spin momenta			
S^{3+}	2.5	2.5	2.5
S^{5+}	2.0 ± 0.1	2.0 ± 0.1	2.0 ± 0.1
Magnetic exchange energies			
J_{AF} (meV)	-3.5 ± 0.2	-3.5 ± 0.2	-5.5 ± 0.3
J_F (meV)	5.1 ± 0.1	5.1 ± 0.1	5.1 ± 0.1
Ratio ($ J_F/J_{AF} $)	1.46 ± 0.05	1.46 ± 0.05	0.93 ± 0.03
Charge-transfer gap			
Δ (meV)	62	58	85

PSFO. The AF exchange in NSFO is comparable to that of the parent *RFO* compounds. Based on Table III and VIII, the increase of $|J_{AF}|$ in NSFO as compared to LSFO and PSFO could arise from differences in the CT gap and/or the lattice distortion of these compounds. The CT gap of NSFO is larger than those of LSFO or PSFO, hence electrons will be more localized, and the magnitude of AF exchange energy of NSFO is expected to increase. In addition, the effect of lattice distortion on the magnetic exchange should also be

considered. The effect of the lattice distortions in the *RFO* parent compounds is well understood. The tolerance factor, whose deviation from 1 indicates the propensity for lattice distortion, decreases from LFO to NFO (see Table II). The larger lattice distortion in NFO results in smaller Fe-O-Fe bond angles that weaken the AF superexchange. The tolerance factor of the *RSFO* compounds is closer to 1 than the parent *RFO* compound and varies only weakly throughout the *RSFO* series. Therefore, the large change in J_{AF} is unlikely to arise

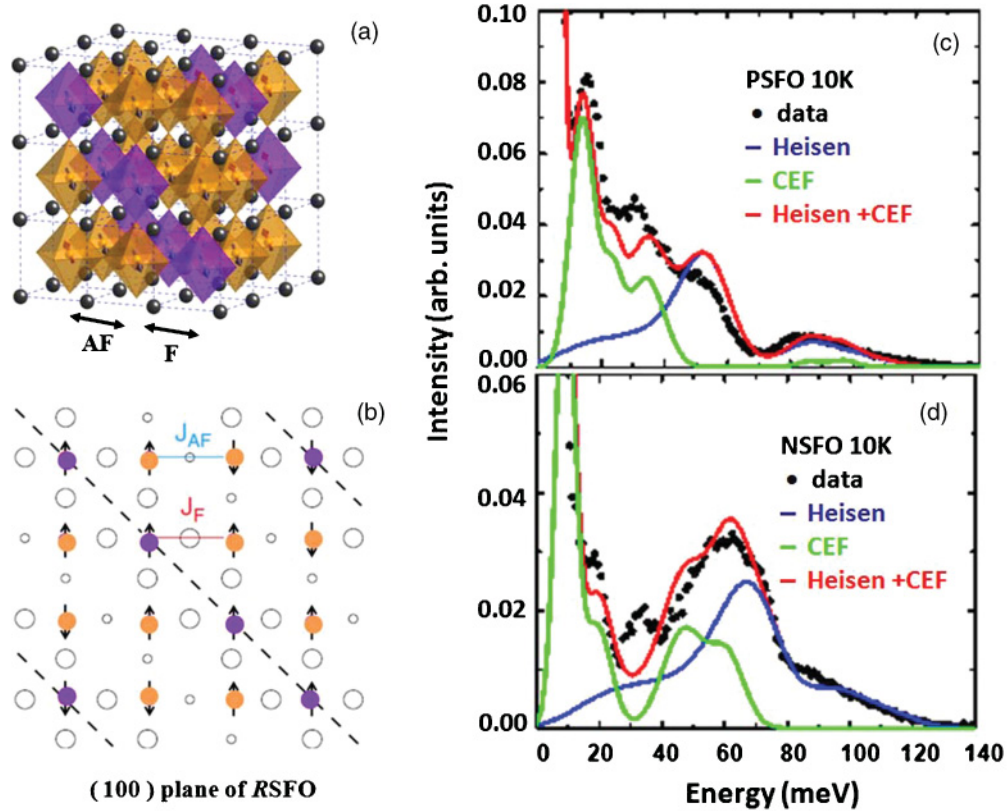


FIG. 8. (Color online) (a) Charge-ordered lattice structure of *RSFO*. Black dots represent R ions. Orange/light (purple/dark) octahedra are $\text{Fe}^{3+}\text{-O}_{6/2}$ ($\text{Fe}^{5+}\text{-O}_{6/2}$). The arrows are the directions of Fe spins. (b) Schematic diagram of oxygen hole density and iron spins in the (100) plane of *RSFO*. Open circles denote oxygen and circle radii represent hole densities. Orange/light (purple/dark) circles are nominal Fe^{3+} (Fe^{5+}) ions. Comparison of *RSFO* [$R =$ (c) Pr and (d) Nd] magnetic scattering spectra on ARCS at 10 K and $E_i = 180$ meV (dots) and summed for 2θ . The Heisenberg model calculations (blue lines), the CEF excitations (green lines), and the sums of the two calculations (red lines) are shown.

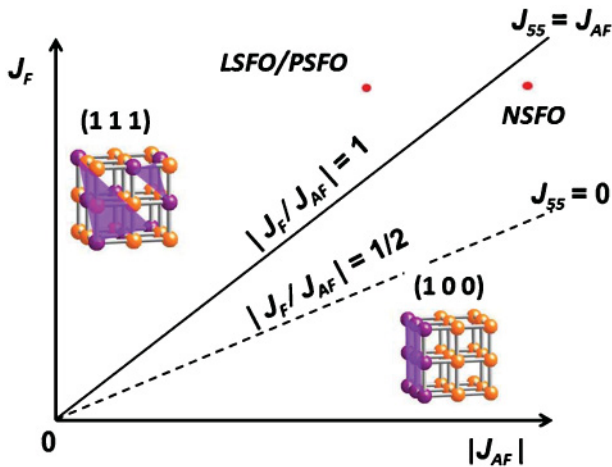


FIG. 9. (Color online) The charged order phase diagram for RSFO ($R = \text{La, Pr, and Nd}$) as a function of nearest-neighbor magnetic exchange. The (111) and (100) types of charge order are illustrated, respectively, in the corresponding portions of the phase diagram.

from an average change of the doping induced structural distortions.

IV. CONCLUSION

Using inelastic neutron scattering, we determined that the similar spin-wave spectra of LSFO and PSFO consist of two energy bands separated by a large energy gap, while the two bands merge into one in NSFO. The full magnetic bandwidth is determined mainly by the ferromagnetic exchange energy J_F between Fe^{3+} and Fe^{5+} ions, and is found to be similar for

the different RSFO compounds. The AF exchange energies between Fe^{3+} ions, $|J_{AF}|$, which controls the splitting of the upper and lower magnetic bands are more sensitive to R substitution. We determine J_F and $|J_{AF}|$ by comparison to a Heisenberg model. The ratio of these exchanges is an indicator of the role that magnetism plays in the formation of the charge-ordered state. While LSFO and PSFO are in the regime where magnetic exchange can stabilize the charge-ordered state, the case for NSFO is not as clear. The much lower exchange ratio in NSFO may come from the increase of the charge-transfer gap that is caused by the smaller Nd ion.

ACKNOWLEDGMENTS

This work was supported by the Division of Materials Sciences and Engineering, Office of Basic Energy Sciences, US Department of Energy. Ames Laboratory is operated for the US Department of Energy by Iowa State University under Contract No. DE-AC02-07CH11358. The work at the Spallation Neutron Source, Oak Ridge National Laboratory (ORNL), was sponsored by the Scientific User Facilities Division, Office of Basic Energy Sciences, US Department of Energy (US DOE). ORNL is operated by UT-Battelle, LLC, for the US DOE under Contract No. DE-AC05-00OR22725. This work has benefited from the use of HIPD and Pharos at the Lujan Center at Los Alamos Neutron Science Center, funded by DOE Office of Basic Energy Sciences. Los Alamos National Laboratory is operated by Los Alamos National Security LLC under DOE Contract DE-AC52-06NA25396.

J.M., J.Q.Y., and R.J.M. thank S. Chang, R. W. McCallum, D. C. Johnston, and P. C. Canfield for the help in sample synthesis and characterization.

*Present address: Oak Ridge National Laboratory, P.O. Box 2008, Oak Ridge, TN 37831, USA.

¹J. M. Tranquada, B. J. Sternlieb, J. D. Axe, Y. Nakamura, and S. Uchida, *Nature (London)* **375**, 561 (1995).

²Z. Jirák, S. Krupička, Z. Šimša, M. Dlouhà, and S. Vratislav, *J. Magn. Magn. Mater.* **53**, 153 (1985); H. Kuwahara, Y. Tomioka, A. Asamitsu, Y. Moritomo, and Y. Tokura, *Science* **270**, 961 (1995).

³C. H. Chen, S.-W. Cheong, and A. S. Cooper, *Phys. Rev. Lett.* **71**, 2461 (1993); S.-W. Cheong, H. Y. Hwang, C. H. Chen, B. Batlogg, L. W. Rupp Jr., and S. A. Carter, *Phys. Rev. B* **49**, 7088 (1994).

⁴J. Q. Li, Y. Matsui, S. K. Park, and Y. Tokura, *Phys. Rev. Lett.* **79**, 297 (1997).

⁵S. K. Park, T. Ishikawa, Y. Tokura, J. Q. Li, and Y. Matsui, *Phys. Rev. B* **60**, 10788 (1999).

⁶R. J. McQueeney, J. Ma, S. Chang, J.-Q. Yan, M. Hehlen, and F. Trouw, *Phys. Rev. Lett.* **98**, 126402 (2007).

⁷T. Mizokawa and A. Fujimori, *Phys. Rev. Lett.* **80**, 1320 (1998).

⁸R. J. McQueeney, J.-Q. Yan, S. Chang, and J. Ma, *Phys. Rev. B* **78**, 184417 (2008).

⁹S. E. Dann, D. B. Currie, M. T. Weller, M. F. Thomas, and A. D. Al-Rawwas, *J. Solid State Chem.* **109**, 134 (1994).

¹⁰R. Kajimoto, Y. Oohara, M. Kubota, H. Yoshizawa, S. K. Park, Y. Taguchi, Y. Tokura, *J. Phys. Chem. Sol.* **62**, 321 (2001).

¹¹D. Treves, *J. Appl. Phys.* **36**, 1033 (1965).

¹²S. M. Shapiro, J. D. Axe, and J. P. Remeika, *Phys. Rev. B* **10**, 2014 (1974).

¹³N. W. Ashcroft and N. D. Mermin, *Solid State Physics* (Brooks-Cole, Belmont, MA, 1976).

¹⁴M. Eibschutz, S. Shtrikman, and D. Treves, *Phys. Rev.* **156**, 562 (1967).

¹⁵G. L. Squires, *Introduction to the Theory of Thermal Neutron Scattering* (Cambridge University Press, Cambridge, England, 1996).

¹⁶S. W. Lovesey, *Theory of Neutron Scattering from Condensed Matter* (Clarendon Press, Oxford, 1984), Vol. 2; W. Marshall and S. W. Lovesey, *Theory of Thermal Neutron Scattering* (Oxford University Press, Oxford, 1971), Chap. 6.

¹⁷E. Prince, *International Tables for Crystallography* (Kluwer Academic Publishers, Dordrecht/Boston/London, 2004), Vol. C, pp. 454–462.

¹⁸A. Podlesnyak, S. Rosenkranz, F. Fauth, W. Marti, A. Furrer, A. Mirmelstein, and H. J. Scheel, *J. Phys. Condens. Matter* **5**, 8973 (1993).

¹⁹R. Przenioslo, I. Sosnowska, M. Leowenhaupt, and A. Taylor, *J. Magn. Magn. Mater.* **140-144**, 2151 (1995).

- ²⁰K. Feldmann, K. Hennig, L. Kaun, B. Lippold, M. M. Lukina, S. Matthies, W. Matz, and E. Warming, *Phys. Status Solidi B* **72**, 817 (1975).
- ²¹A. Podlesnyak, S. Rosenkranz, F. Fauth, W. Marti, H. J. Scheel, and A. Furrer, *J. Phys. Condens. Matter* **6**, 4099 (1994).
- ²²P. D. Battle, T. C. Gibb, and P. Lightfoot, *J. Solid State Chem.* **84**, 271 (1990).
- ²³Y. M. Zhao, M. Hervieu, N. Nguyen, and B. Raveau, *J. Solid State Chem.* **153**, 140 (2000).
- ²⁴J.-S. Zhou and J. B. Goodenough, *Phys. Rev. B* **77**, 132104 (2008).